Detecting the Debris of Solar System Formation Via Stellar Occultation

A Senior Honors Thesis

Presented in Partial Fulfillment of the Requirements for graduation
with research distinction in Astronomy in the undergraduate
colleges of The Ohio State University

by

Garrett T. Elliott

The Ohio State University
May 2008

Project Advisor: Professor B. Scott Gaudi, Department of Astronomy

ABSTRACT

The distant belt of icy objects beyond the orbit of Neptune constitute the leftover construction debris of our solar system's formation, and their physical properties provide key insights to the processes at work in planet formation. Traditionally, these objects have been detected directly via sunlight reflected from their surfaces. This standard method is hindered by the objects' large distances (40 to 10,000 times further from the Sun than the Earth) and small sizes (tens to hundreds of kilometers). Observing the occultation of stars as these objects pass in front provides an alternate method for detecting these objects, bypassing this current impasse to their discovery. When debris crosses in front of a fixed background star, the apparent brightness of the star will be reduced as it is shielded from Earth's view. The magnitude of the brightness diminution depends on the size of the occulter, the apparent size of the star, the Fresnel scale which determines the magnitude of diffraction effects, and the minimum angular separation between the object and the star. The quality of the observation is of course constrained by the detector's sensitivity and sampling rate. By developing a mathematical model, which accounts for all these parameters, the maximum detectable separation between the star and occulter can be determined to produce predictions for the approximate number of potential stellar occultation observations, once paired with the population and size distribution of objects. These two quantities are the unknown and desired functions that can be inferred by a number of stellar occultation events. This model will be applied to the parameters of ongoing and planned occultation surveys to estimate their expected yields, as well as determine whether binary objects, which can provide additional information about planet formation, can also be routinely detected. Support for this project was provided through the Astronomy Depart-

ment's Summer Undergraduate Research Program.

Subject headings: Kuiper Belt - Oort Cloud - solar system - stellar occultation

1. Introduction

Our efforts to understand the contents and formation history of the solar system were advanced significantly in 1992 with the discovery of a population of objects with orbits beyond that of Neptune (Jewitt & Luu 1993). Several thousand such trans-Neptunian Objects (TNOs) are now known to exist in a region of the solar system once observationally devoid of bodies other than Pluto and Charon. These TNOs, also known as Kuiper Belt Objects (KBOs)[1], which together comprise a total of about one lunar mass of material (Bernstein et al. 2004), are bodies of rock and ice with typical sizes of ~ 100 km, and masses of less than a millionth the mass of the Earth. Larger bodies are known to be considerably rarer, with the number of bodies as function of size r varying as a power law as r^{-q}, with $q \sim 4$ (Bernstein et al. 2004). Below ~ 100 km, the size distribution is expected to flatten. There is observational evidence for this, although the constraints are poor owing to the faintness of these small bodies.

Though distant and small, KBOs do in fact play a roll in inner solar system happenings. It is currently believed that the kilometer-sized Jupiter Family Comets (JFCs) are relatively recent escapees from the Kuiper Belt (Duncan et al. 1988). These objects are constantly being perturbed by the giant planets. Thus their orbits are dynamically unstable, and over a timescale that is short compared to the age of the solar system, they are ejected from the solar system, or sent careening into the Sun or the inner planets. Therefore the existence of JFCs today requires a large reservoir from which they can be constantly replenished. Current theories suggest that the supply rate is simply proportional to the number density of objects in the reservoir, which is generally thought to be the Kuiper Belt. However, the progenitors of JFC are only a kilometer in size, and objects this size cannot be directly

[1]We will refer to all objects outside of Neptune's orbit only as TNOs unless specifically discussing those orbiting from 30-55AU.

detected at the distances of the Kuiper Belt. Thus the hypothesis that the Kuiper Belt is the reservoir of JFCs has yet to be confirmed.

Studying TNOs, which likely constitute the leftover 'construction debris' of planet formation in the solar system, can also shed light on the dynamical history of the planets. For example, examination of the detailed dynamical populations of KBOs indicates that Neptune likely migrated outward early in the solar system's history, thereby capturing some KBOs (such as Pluto) into mean-motion resonances with it, and throwing others into orbits with higher inclinations and eccentricities (Malhotra 1995). Others have also theorized that KBOs perturbed into Earth-crossing orbits during the formation of outer planets could have provided the source of the impactors during the heavy bombardment periods on the Earth (Levison et al. 2001).

At the edge of the solar system, the Oort cloud is theorized to be a much more distant region of planetary debris at distances of $10^4 - 10^5$ AU, that is populated with objects that were ejected to the far ends of the solar system by perturbations from the outer planets. Theories identify this region as the most likely source of long period comets (Oort 1950). Direct observations of bodies in the Oort Cloud remain unsuccessful because the objects are so distance and thus faint.

A more thorough study of the Kuiper Belt and outer solar system objects in general will yield better estimates of the number density and size distribution of the smaller (one to hundreds of kilometers) objects. This will then help to confirm if JFCs are coming from the Kuiper and if not it will generate further intrigue into the source of the JFCs, possibly implicating the theorized Oort Cloud. The investigation will also inform better numerical simulations for explaining the dynamical history of the solar system. Direct detection of Oort cloud objects would of course confirm the existence of this enigmatic structure in the very outer regions of our solar system.

Unfortunately, standard methods can only be routinely used to discover TNOs with radii $\geq$ 100 km and distances of $\lesssim$ 100 AU, thus limiting our ability to address these questions. This limitation is intrinsic to the method by which these objects are currently detected, namely the direct detection of reflected sunlight off their surfaces. This technique eventually fails for distant TNOs because the flux from any object drops by $distance^2$, so for a two way trip from the Sun to a TNO and back to the Earth the flux drops by $distance^4$. Similarly, it is difficult to detect small objects, as the reflective surface area varies as $radius^2$. These limitations are exacerbated by the fact that the TNOs have apparent sky motions of $\sim 3''$ hr^{-1}, and thus it is not possible to simply increase the exposure times indefinitely to collect more photons, as the reflected light from the TNO will be smeared over many resolution elements, thus degrading the sensitivity. These difficulties can be ameliorated by using sophisticated 'digital tracking' techniques, in which many images are shifted by the amount expected for objects moving at the rates anticipated for TNOs, and then added to increase the sensitivity, but there is nevertheless a practical limit to the smallest or most distant TNO that can be detected from a given telescope using this approach.

An alternative approach to direct detection of reflected sunlight is stellar occultations. In this method one searches for the diminution, or occultation, of distant background stars as a TNOs passes in front. Since even very small, kilometer-sized TNOs can result in significant occultations, this method can be used to discover objects that are much smaller than can be found via direct detection. Furthermore, the distance of the TNO plays only a secondary role in the magnitude of the diminution, and so objects can be found with distances quite far from the sun. By observing these serendipitous occultations, and accounting for the diffraction effects due to the wave nature of light, one can derive useful information about the occulting object. The abundance of background stars makes the detection of numerous $\gtrsim 1$ km sized TNOs from occultation feasible.

In practice the easiest observable from occultation surveys is the detection rate. This depends on the surface density and size distribution of the TNOs, as well as the photometric accuracy and sampling rate of the occultation survey. Cooray & Farmer (2003) estimated detection rates for occultation surveys by assuming a power-law distribution of TNO sizes, with a turnover below a critical radius of $\lesssim 100$ km. Although these authors did acknowledge the importance of diffraction effects, and in particular note the increased detectability of occultations due to these effects for experiments with sufficient photometric precision, they do not self-consistently compute how photometric precision affects the detectability when diffraction effects are considered. Nihei et al. (2007) does consider these effects, and additionally tests detectability with several finite sources sizes and sampling rates. However, this study only considered occultation events for which the center of the TNO passes directly over the center of the background star, i.e. they only consider events with zero impact parameter.

We improve upon previous work by computing the detectability of occultation light curves, self-consistently considering the effects of diffraction, the finite size of the star, the photometric precision, and the sampling rate, and allowing for nonzero values of the impact parameter. We use calculations and analysis of occultation events over a wide region of parameter space to derive at approximate fitting formula for the maximum impact parameter that allows for an event to be detected. This fitting formula, when applied to a given occultation survey, and combined with a model for the size and distance distribution of occulting objects, can then be used to estimate realistic detection rates.

The next section provides a review of the primary physical parameters that affect the morphology of occultation events and thus determine their detectability. We then show how the maximum impact parameter can be combined with a model for the size and distance distribution of KBOs to predict the detection rate for occultation surveys. In §5

we compute, for a wide span of these physical parameters, the maximum impact parameter for which a TNO can be detected, for a given sampling rate and photometric precision. We also derive an analytic fitting formula for this maximum impact parameter as a function of the physical parameters, photometric precision, and sampling rate. Finally, we summarize our results and conclude.

2. Parameters

The morphology and duration of an occultation event depend on the several physical parameters, as well as several parameters of the observational setup. The physical parameters are the radius of the TNO r, and the distance of the TNO from the Earth D. The finite size of the source may also play a role, which we parameterize by $R_* = D\theta_*$, where θ_* is the angular size of the source, which can be estimated from its color and flux. The important parameters of the experimental setup are the wavelength of the observations λ, which together with D set the scale of the diffraction effects, and the time resolution over which the light curve is integrated. We now consider several different limits of the morphology of occultation events.

2.1. Simple Geometric Occultation Events

In the simplest case of a geometric occultation with a small source, which holds for large and nearby occulters (we define this precisely later), one has a simple, boxcar, total eclipse. Light curves in this case are specified by a single parameter, the timescale of the event, which from a simple geometrical analysis, is given by

$$\Delta T = \frac{2r}{v_{\rm T}}\sqrt{1-\left(\frac{B}{r}\right)^2}, \tag{1}$$

where B is the impact parameter of the event, and v_T is the TNO's apparent transverse velocity, which depends on its own velocity as well as the reflex velocity of the Earth. For circular motion of the Earth and TNO, the transverse velocity is,

$$v_{\rm T} = v_{\oplus} \left(\cos\phi - \sqrt{\frac{\rm AU}{D} \left(1 - \frac{\rm AU}{D} \sin\phi \right)^2} \right), \tag{2}$$

where ϕ is the phase angle of the TNO, $v_{\oplus}$ is the velocity of the Earth. At opposition,

$$v_{\rm T} = v_{\oplus} \left(1 - \sqrt{\frac{\rm AU}{D}} \right). \tag{3}$$

In the geometrical occultation limit, it is not possible to determine the radius and distance to the TNO separately, because the only observable, ΔT, depends on B, r, and D, which are not known *a priori*. It is possible to break this degeneracy by making two observations along the path of the occultation but at separate locations. For kilometer-sized KBOs this only requires a separation of a few kilometers (Cooray 2003).

2.2. Diffraction and Finite Source Size Effects

For small or distant TNOs, effects due to diffraction of light and the finite size source star will affect the morphology of the light curve.

The degree of diffraction depends on the radius of the TNO relative to the Fresnel scale, r_f,

$$r_f = \sqrt{\frac{D\lambda}{2}}. \tag{4}$$

A proper treatment of the effects of diffraction would require integrating over the bandpass of the detector's filter, which would generally suppress the diffraction effects. However, for a bandwidth of $4000\mathring{A} - 8000\mathring{A}$, the effect is minimal (Nihei et al. 2007), and so we will simply assume monochromatic light with a wavelength of $5500\mathring{A}$.

Including diffraction effects, the relative flux $I_{\rm ps}(x,r)$ of a circular occulter of radius r, whose center is a distance x from a point source, is given by (Roques et al. 1987),

$$I_{\rm ps}(\eta) = \begin{cases} U_0^2(\eta,\rho) + U_1^2(\eta,\rho) & \eta \le \rho \\ 1 + U_1^2(\rho,\eta) + U_2^2(\rho,\eta) & \eta \ge \rho \\ \quad -2U_1(\rho,\eta)\sin\frac{\pi}{2}(\rho^2+\eta^2) & \\ \quad +2U_2(\rho,\eta)\cos\frac{\pi}{2}(\rho^2+\eta^2) & \end{cases}, \tag{5}$$

where,

$$U_n\ (\mu,\nu) = \sum_{k=0}^{\infty} (-1)^k (\frac{\mu}{\nu})^{n+2k}\ J_{n+2k}(\pi\mu\nu), \tag{6}$$

and,

$$\rho = \frac{r}{r_f}, \qquad \eta = \frac{x}{r_f}. \tag{7}$$

When $\rho \gg 1$, the light curve converges to that of the simple, geometric, boxcar form.

The effect of the finite size of the source is to average the flux over the area of the source,

$$I_{\rm fs}(x) = \frac{1}{\pi r_*^2} \int_0^{2\pi} \int_0^{r_*} r'_* dr'_* d\phi\, I_{\rm ps}(x^2 + r'^2_* + 2xr'_*\cos\phi), \tag{8}$$

where we have assumed a uniform surface brightness of the source.

2.3. Regimes of Light Curve Morphology

The parameters $r,\ r_f$, and r_* entirely predict the morphology of an occultation light curve, and thus the detectability for a given observational setup. Figure 1 displays a plot of r vs. D, which we can divide into four regimes based on light curve morphology. We can divide the plot horizontally into sides A/D and B/C based on the distance where $r_* = r_f$, which is given by,

$$D_{div} = \frac{\lambda}{2\theta_*^2}, \tag{9}$$

which for a $V = 12$ A0V star is roughly equal to $D_{\rm div} \simeq 2500$ AU. For $D < D_{div}$ diffraction effects will dominate over finite source effects, whereas for $D > D_{div}$, the opposite will be true.

Each half can then be divided into two regimes depending on whether or not the relevant effect (diffraction for A/D or finite source for B/C) is important. For region A, the size of the TNO is larger than the Fresnel scale ($r > r_f$), and thus diffraction effects are subdominant. Conversely, for region D, $r < r_f$, and diffraction effects are important. For region B, $r > r_*$, and finite source effects are subdominant, whereas for region C, $r < r_*$, so finite source effects are important.

Example occultation light curves which illustrate the different possible morphologies are shown, for the case of a V = 12 A0V source, in Figure 2.

The light curve in quadrant A, denoted by position "1", demonstrates the closest relation to the "boxcar" regime, when $r \gg r_*, r_f$, although still retains significant diffraction wings and a central Poisson peak. Similarly, quadrant B's light curve, position "2", is also close to the boxcar regime, but here the finite size of the source is still significant. The light curve in quadrant C is shallow and broad because only a fraction of the source is occulted. Once back in the Fresnel dominated regime of quadrant D, the finite source size is much less important, but the diffraction effects are dominant. In this case the original boxcar shape is barely discernible, and the light curve resembles essentially a broad, shallow wave pattern due to diffraction. The remaining light curve in Figure 2 is produced at the intersection of all four quadrants where $r_*/r_f \sim 1$ and $r/r_f \sim 1$. Here both diffraction and finite source effects are significant, as is reflected in the light curve morphology.

It is clear that, for occultation events with parameters close to the dividing lines between regimes A/D and B/C, the detectability will be somewhat enhanced over the simple boxcar regime due to the longer event durations, but for occultation events deep in

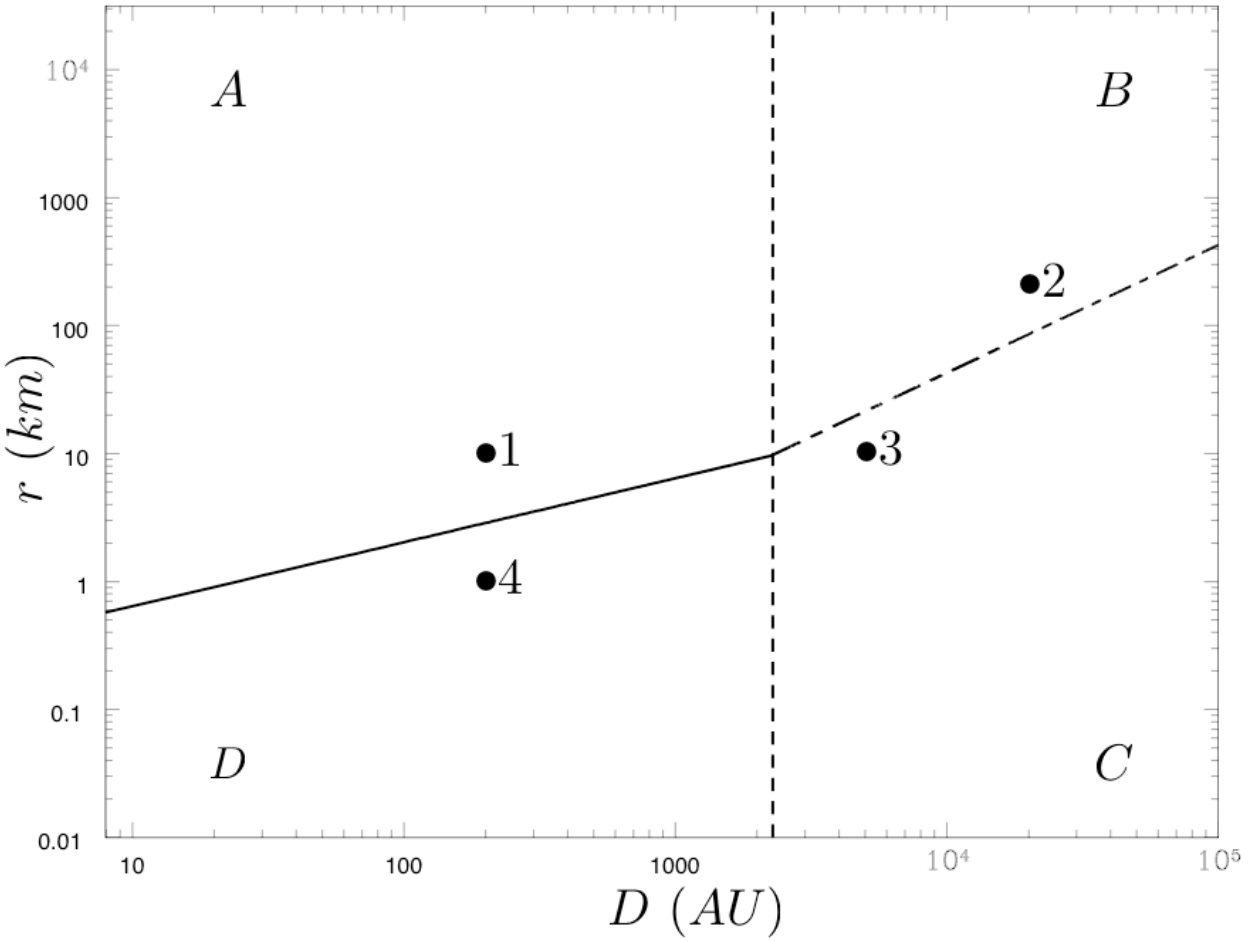

Fig. 1.— Four quadrants (A,B,C,D) are produced on a r vs. D plot by varying the parameters r_* and r_f for a V = 12 A0V star. A/D represents the fresnel dominated regime and B/C is dictated by the projected source size. A/D is divided by the relation of $r = r_f$ (solid line) and B/C by $r = r_*$(long-short dashed line). The quadrants intersect at $r_* = r_f = r$. Example light curves corresponding to positions 1-4 and the intersection are depicted in Figure 2.

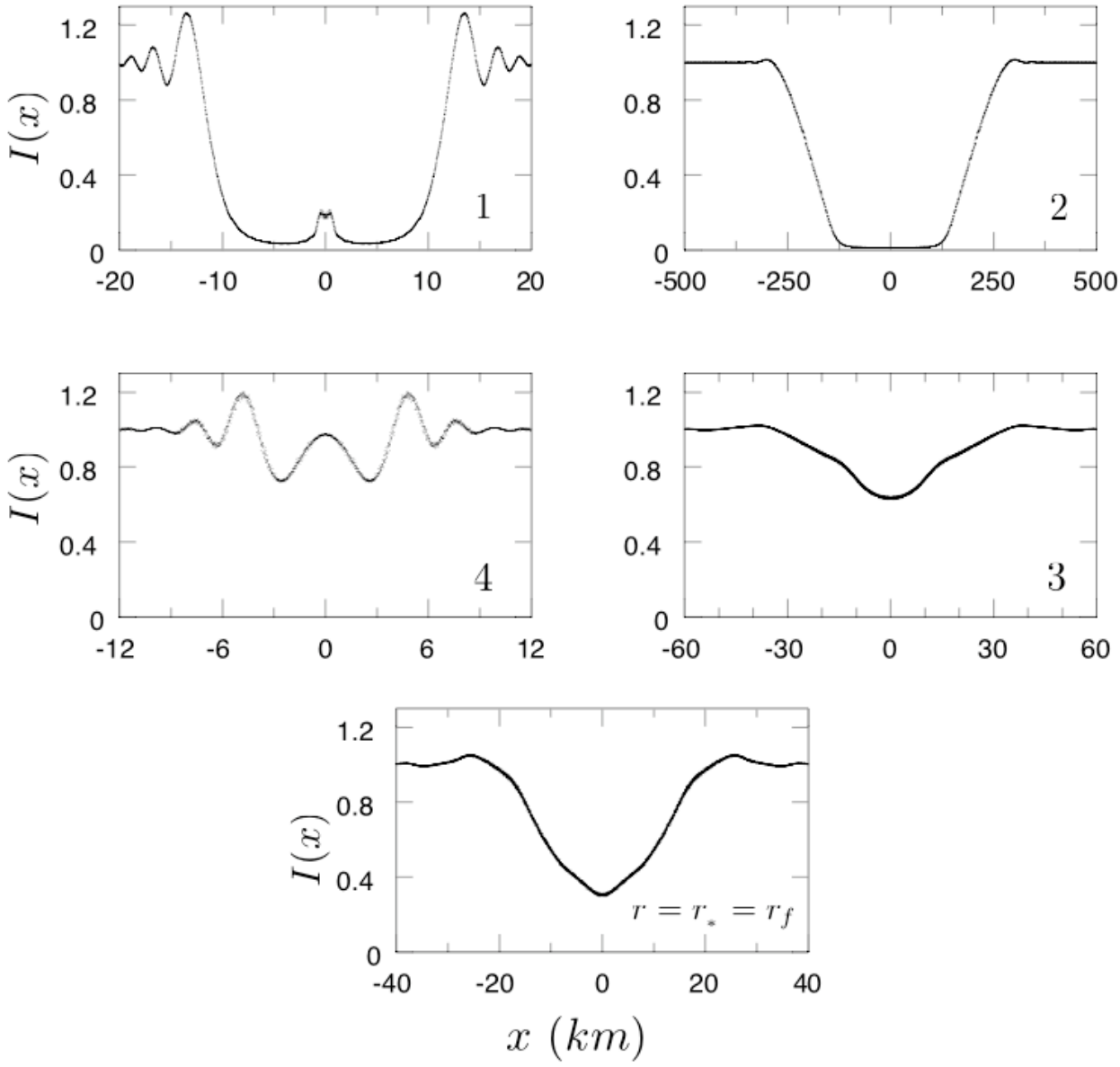

Fig. 2.— Five light curves derived from the parameters at positions 1-4 and the quadrant intersection in Figure 1 for a V = 12 A0V star and B = 0.

the D or C regimes, the detectability will be strongly suppressed, due to either diffraction or finite source effects strongly depressing the flux variability.

2.4. Finite Sampling

Detectors must sample at a finite rate, and integrate for a finite amount of time. Given the relatively brief event duration for some parameter combinations ($\Delta T \lesssim 1$ s), the effect of finite sampling and integration times can be quite important. We assume that the sampling rate of a detector measures the frequency, f, at which a new exposure can be taken. We assume no loses between exposures, and so f^{-1} is also the integration time per exposure. During one exposure, the variations in intensity will be integrated over and binned together during the exposure time. These bins correspond to a integration length r_{bin} of

$$r_{bin} = \frac{v_{\rm T}}{f}. \tag{10}$$

In order for an event to be detectable, r_{bin} must be less than the characteristic event length scale. For example, in the boxcar regime, $r_{bin} \lesssim v_{\rm T}\Delta T$. If this is not satisfied, the event will be entirely integrated over, and so detection is effectively impossible. Even in cases where $r_{bin} \sim v_{\rm T}\Delta T$, only mere detection is possible, and it will be difficult to characterize the event. Thus for proper characterization, the experimental setup must satisfy $r_{bin} \ll v_{\rm T}\Delta T$.

Figures 3 and 4 show the example light curves in Figure 2, now including the effects of finite sampling rates with $f = 40Hz$ and $5Hz$.

3. Analysis

Consider a TNO with a radius r moving at a velocity v_T. Now assume that this TNO will produce a detectable event provided that it passes within a distance B_{max} of a

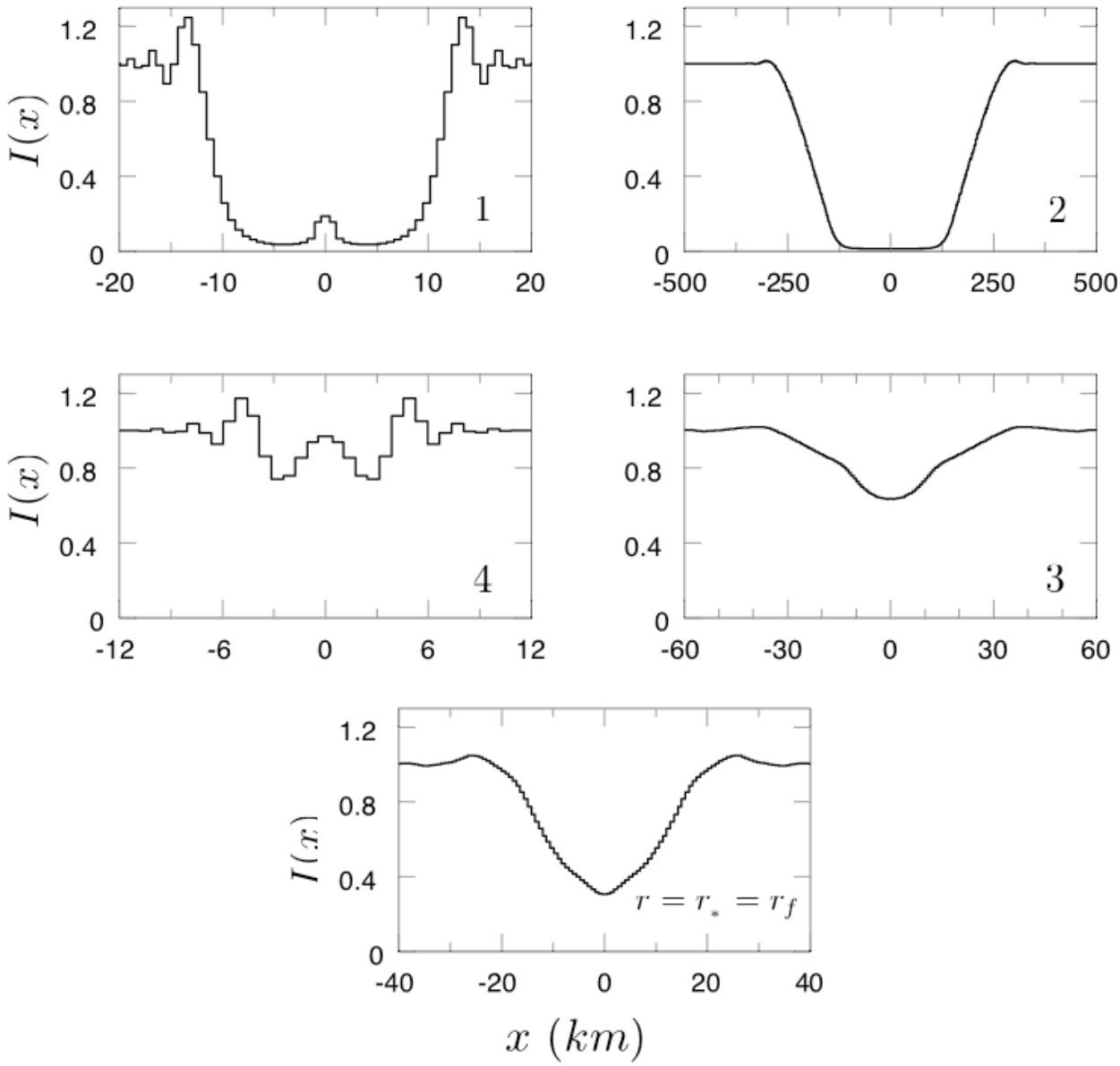

Fig. 3.— The five light curves from Figure 2 when observed at a $40Hz$ sampling rate. The diffraction effects are still apparent, $r_{bin} < v_{\rm T}\Delta T$ in all regimes.

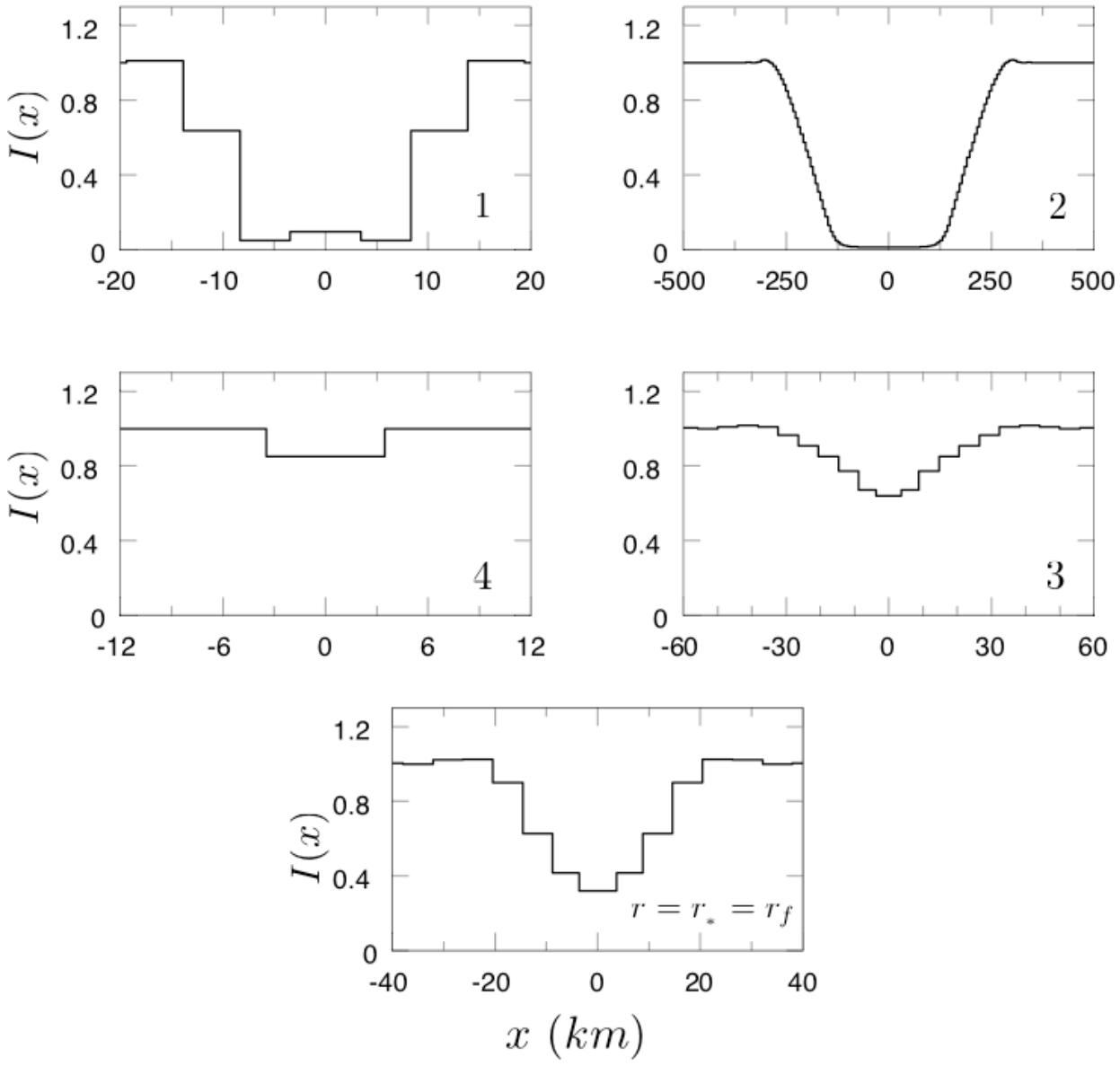

Fig. 4.— The five light curves from Figure 2 when observed at a $5Hz$ sampling rate. The diffraction effects are drastically reduced, $r_{bin} \sim v_{\rm T}\Delta T$ in the A/D regime.

star. The total area swept out by the TNO in which a star would give rise to a detectable occultation event over the survey lifetime L is then given by $2v_T L B_{max}$.

Now consider a population of identical TNOs with surface density n_{TNO}. The total number of TNOs in a field of view, with area A_{FOV}, would be $n_{TNO} A_{FOV}$. The total detectable area covered by all the TNOs in the field of view is then,

$$A_{TNO} = 2v_T L B_{max} n_{TNO} A_{FOV}. \tag{11}$$

Finally, for a surface density of stars n_*, the total number of detected occultation events during the survey lifetime is,

$$N_{det} = n_* A_{TNO} = 2v_T L B_{max} n_* n_{TNO} A_{FOV}. \tag{12}$$

Of course, this analysis assumes a uniform population of TNOs and stellar targets, but extending the discussion to include a distribution of TNO sizes, distances, and stellar properties is trivial.

The simplest observable from occultation surveys is the number of detected occultation events, N_{det}. From the previous discussion, it is clear that

$$N_{det} \propto B_{max} n_{TNO}. \tag{13}$$

Thus with a proper calibration of B_{max}, the observed detection rate can be used to estimate the surface density of TNOs. Similarly, assuming a model for the surface density of TNOs, an estimate of B_{max} for a proposed survey can be used to estimate the expected detection rate.

Our goal is to provide a simple, analytic fitting formula for B_{max} which can be used to estimate the expected yield of occultation surveys. To do this, we compute occultation curves over a large span of parameter space using the procedures discussed in § 2. We then estimate their detectability as a function of impact parameter B and use this to numerically determine B_{max}. Finally, we fit these numerical results to a simple analytic formula.

4. Detection

The detectability of a given occultation light curve depends on the photometric precision of the experimental setup (telescope, detector, etc). We determine whether or not a given light curve would be detectable in an occultation survey by determining its root-mean-square (RMS) variation about a constant light curve, and then asking whether this RMS is larger than some minimum $\mathrm{RMS}_{\mathrm{min}}$ required for detection.

The normalized root mean square of an occultation event is,

$$\mathrm{RMS} = \sqrt{\frac{1}{N}\sum_{i}^{N}[1 - I_{fs}(t_i)]^2}, \tag{14}$$

where N is the total number of points, each taken at time t_i.

The minimum RMS required for detection for a given occultation survey can be estimated assuming that each point has a photometric uncertainty σ. Then,

$$\mathrm{RMS}_{\mathrm{min}} = \frac{\sigma}{N^{1/2}}. \tag{15}$$

Thus, $\mathrm{RMS}/\mathrm{RMS}_{\mathrm{min}} \sim 3$ corresponds to roughly a 3-σ detection.

5. Results

In this section, we explore how the detectability depends on the impact parameter B, Fresnel scale r_f, and source size r_*. In particular, we determine that maximum impact parameter B_{max} at which a occulter can pass a given star and still be detected, as a function of r_f, r_*, and RMS_{min}.

To give a qualitative sense of how B_{max} is computed, Figure 5 shows several light curves where we have kept the physical parameters constant, but increased the impact parameter, for the case when $r = r_f$ and $r \gg r_*$. We see that, as B increases, the amplitude of the

flux variations decreases, although it is clear the behavior is not trivial (and, as we will see, non-monotonic).

For simple geometric occultation event ($r \gg r_f, r_*$), we can derive an analytic expression for the variation of the RMS with impact parameter Equation (1),

$$\mathrm{RMS} \propto \left(1 - \left(\frac{B}{r}\right)^2\right)^{1/4}. \tag{16}$$

Figure 6 shows the RMS as a function of B for an occulter and source star with physical parameters such that it is very nearly in the geometric regime (r =100 km, D =40 AU, and $r_* \ll r$). We see that the variation with B is as expected: the RMS is exactly one at zero impact parameter and drops nearly to zero at the radius of the TNO. The small tail of finite RMS beyond $B = r$ is caused by diffraction effects, which are small because $r \gg r_f$, but nevertheless present at a low level.

This approximation is, however, only correct in the limit of $r \gg r_*, r_f, r_{bin}$, and will break down when the effects of diffraction, finite source effects, and finite sampling are included. A direct computation of the RMS for individual light curves in all regimes is required for the further analysis. We are aided somewhat in computation speed because the interference pattern is circularly symmetric. Thus, we can compute light curves for $B = 0$, and then extend these to nonzero impact parameters using,

$$I_{fs}(x; B \neq 0) = I_{fs}(y; B = 0) \text{ , where } y = \sqrt{x^2 + B^2}. \tag{17}$$

To arrive at the maximum impact parameter we first measure the RMS of numerous light curves that were each incremented in B. Figure 7 depicts the RMS values for occultation events with distinct background stars and a Fresnel scale corresponding to $D = 40AU$. In the limit of longer impact parameters and larger stellar disks, the RMS approaches zero because the occulting object only minimally diminishes the background star's flux. Large sources with $r_* > r_f$ also smooth out the diffraction features.

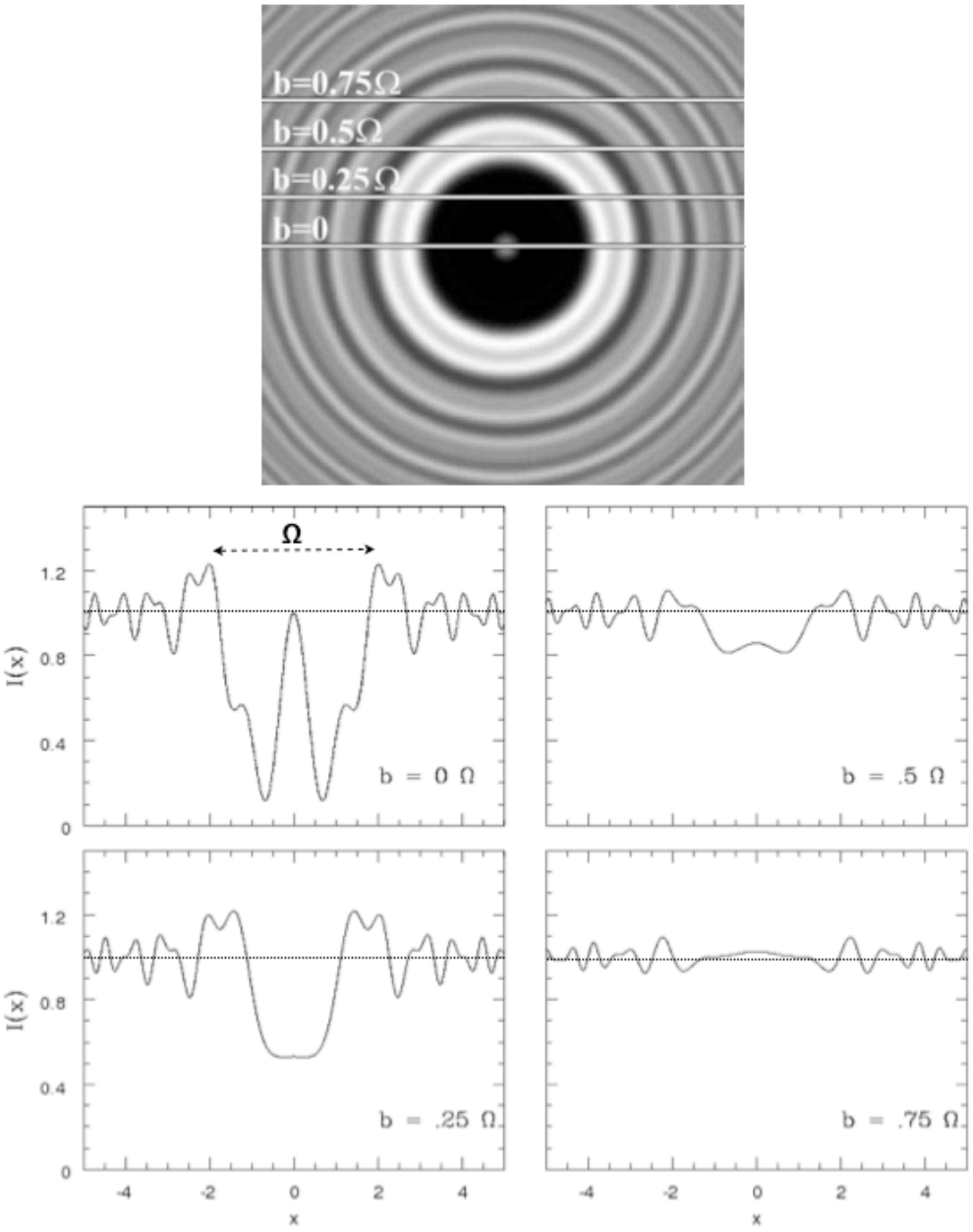

Fig. 5.— The upper most plot is the projected occultation pattern for a point source, where $r/r_f = 1$ (Nihei et al. 2007). This pattern shows the relative flux as a function of source position, where whiter regions are larger positive deviations. The four lower plots show light curves produced by this geometry, which are simply cross sections through the circularly symmetric occultation patter. The nonzero impact parameters, B, are listed in the lower corner of the light curves. The impact parameter is scaled in units of the width Ω of the occultation event for $B = 0$.

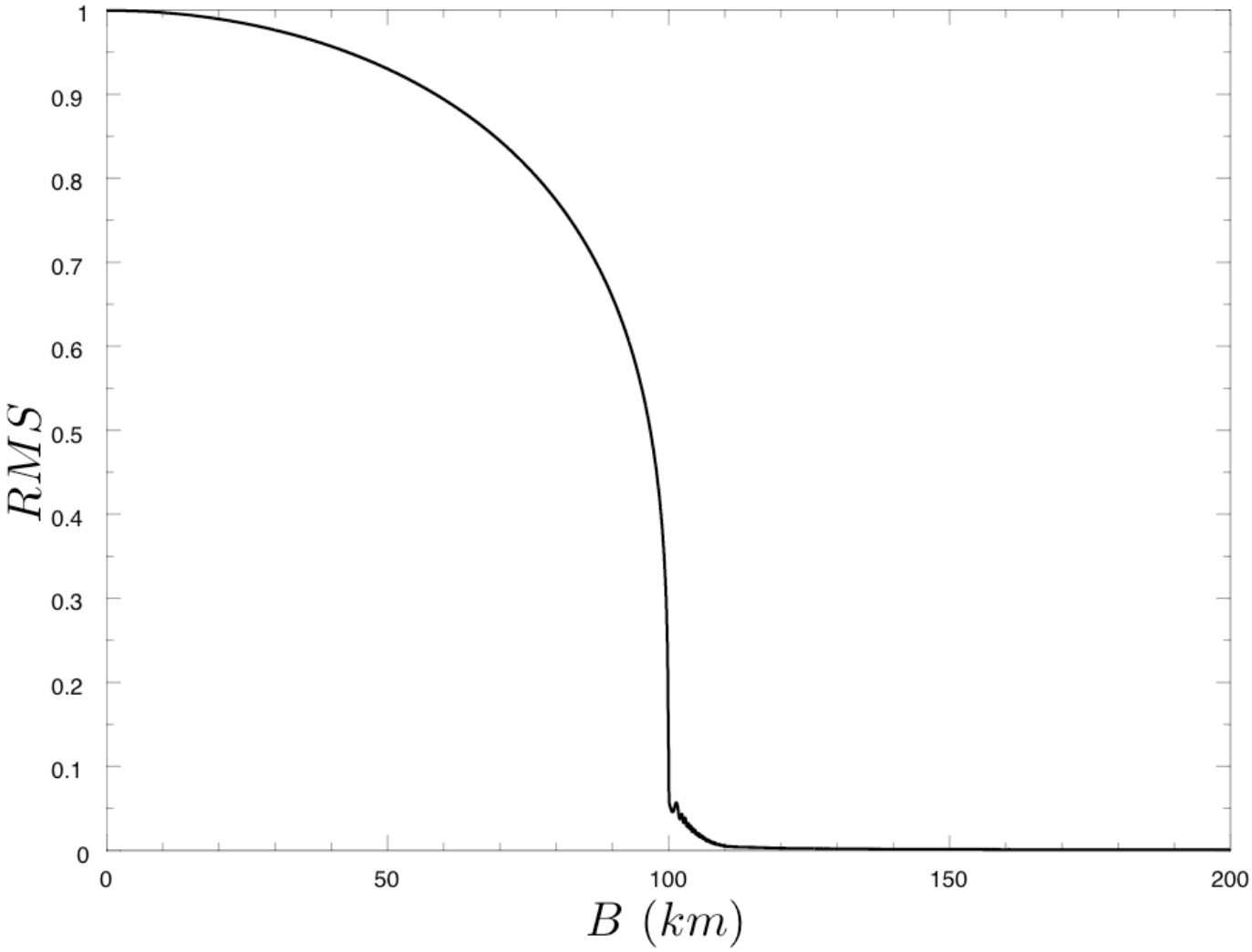

Fig. 6.— The RMS of a simple geometric occultation light curve follows a $(1-(B/r)^2)^{1/4}$ relation. The RMS approaches zero at the TNO's radius. The TNO is a 100km KBO at 40 AU occulting a V = 12 A0V star.

The maximum impact parameter is determined by choosing a constant RMS and then locating the first impact parameter value on a RMS vs. B curve, of constant r_f, whose light curve RMS is greater than or equal to the constant value. Because the RMS versus B functions are non-monotonic, the light curve RMS value may again drop below the constant. However, we defined B_{max} as the first instance of equality. We then increment the Fresnel scale and repeat the analysis. Figure 8 shows B_{max} as a function of r_f/r for various values of the RMS, assuming infinite sampling and a point-like background star. We also computed B_{max} as a function of r_{bin}, which we do not show here.

Finally, we fit the curves in Figure 8. The features of the the fit include a break point in r_f/r, where for larger r_f/r the $B_{max} \propto r_f$, as well as a cutoff at increasingly larger r_f/r. The break, r_b, and cutoff, r_c, are predicted by the equations

$$r_b = r\left(b_1\frac{r_*}{r_f} + b_2\frac{r_{bin}}{r_f} + b_3\mathrm{RMS}^{\nu}\right) \tag{18}$$

and

$$log_{10}\left(\frac{r_c}{r}\right) = c_1 + c_2 log_{10}(\mathrm{RMS}) - Exp\left[\frac{1}{(1-\mathrm{RMS})^{c_3}}\right], \tag{19}$$

where constants b_i, c_i, and ν are real numbers. With these features defined, the functional form of B_{max} is

$$B_{max} = \left\{\left(\sqrt{1-\mathrm{RMS}^4}\left(1+\frac{r_*}{\alpha r}\right)Exp\left[-\frac{r_*}{\beta r}\right]Exp\left[-\frac{r_{bin}}{\gamma r}\right]\right)^{\frac{1}{s}} + \left(\frac{r_f}{r_b}\right)^{\frac{1}{s}}\right\}^{s} \tag{20}$$

and the scaling parameters (α, β, γ) are actually linear functions of the RMS in the form of

$$\begin{aligned} \alpha &= A + B(\mathrm{RMS}) \\ \beta &= C - D(\mathrm{RMS}) \\ \gamma &= E - F(\mathrm{RMS}) \end{aligned} \tag{21}$$

with positive real numbers as constants A-F.

We note that in the limit of $r \gg r_*, r_f, r_{bin}$, B_{max} does take the form of $\sqrt{1-\mathrm{RMS}^4}$ as predicted.

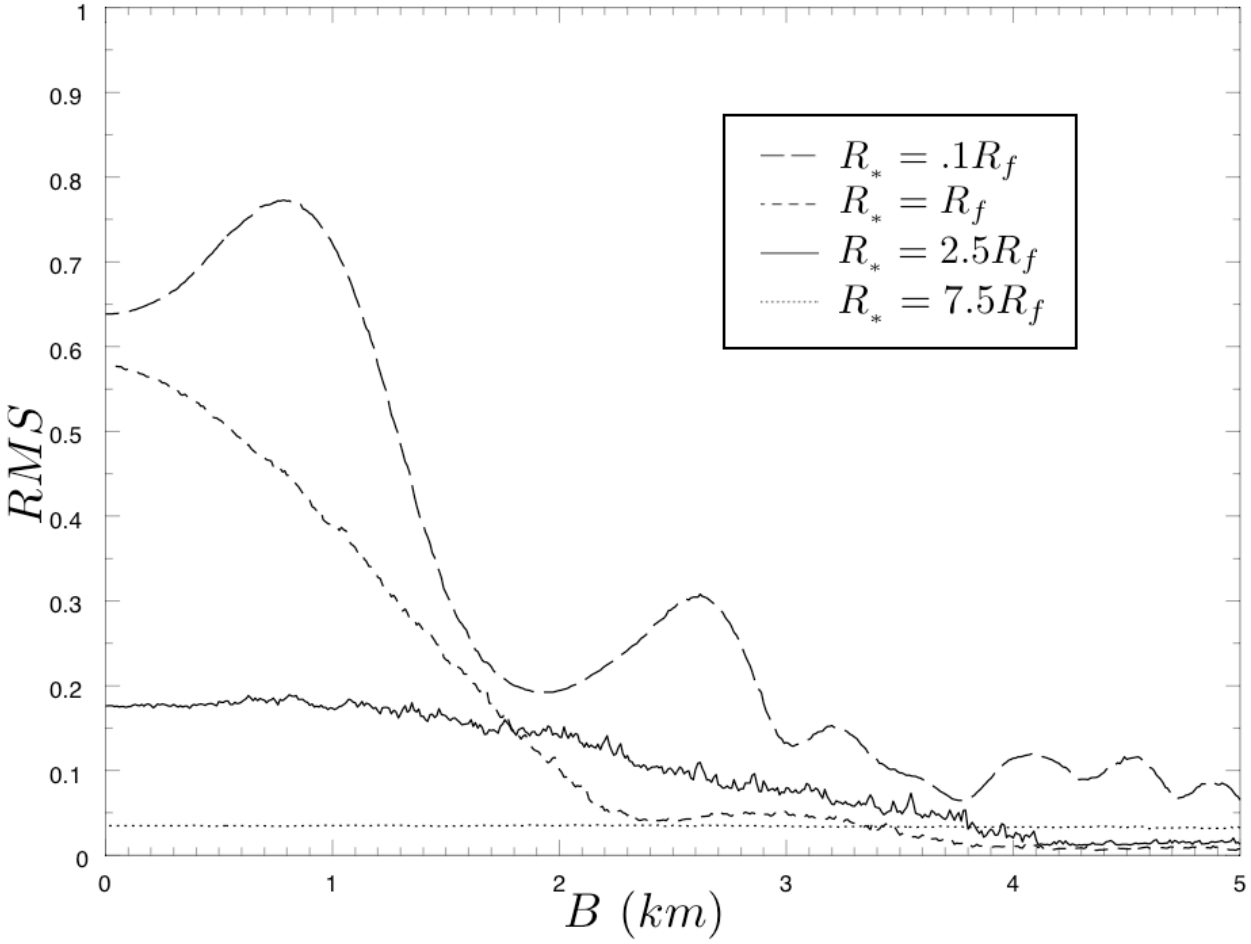

Fig. 7.— RMS calculations for background stars of various angular size, listed in the legend in terms of the Fresnel scale. For this scenario the TNO is a 1km KBO at 40AU and the detector has a $40Hz$ sampling rate.

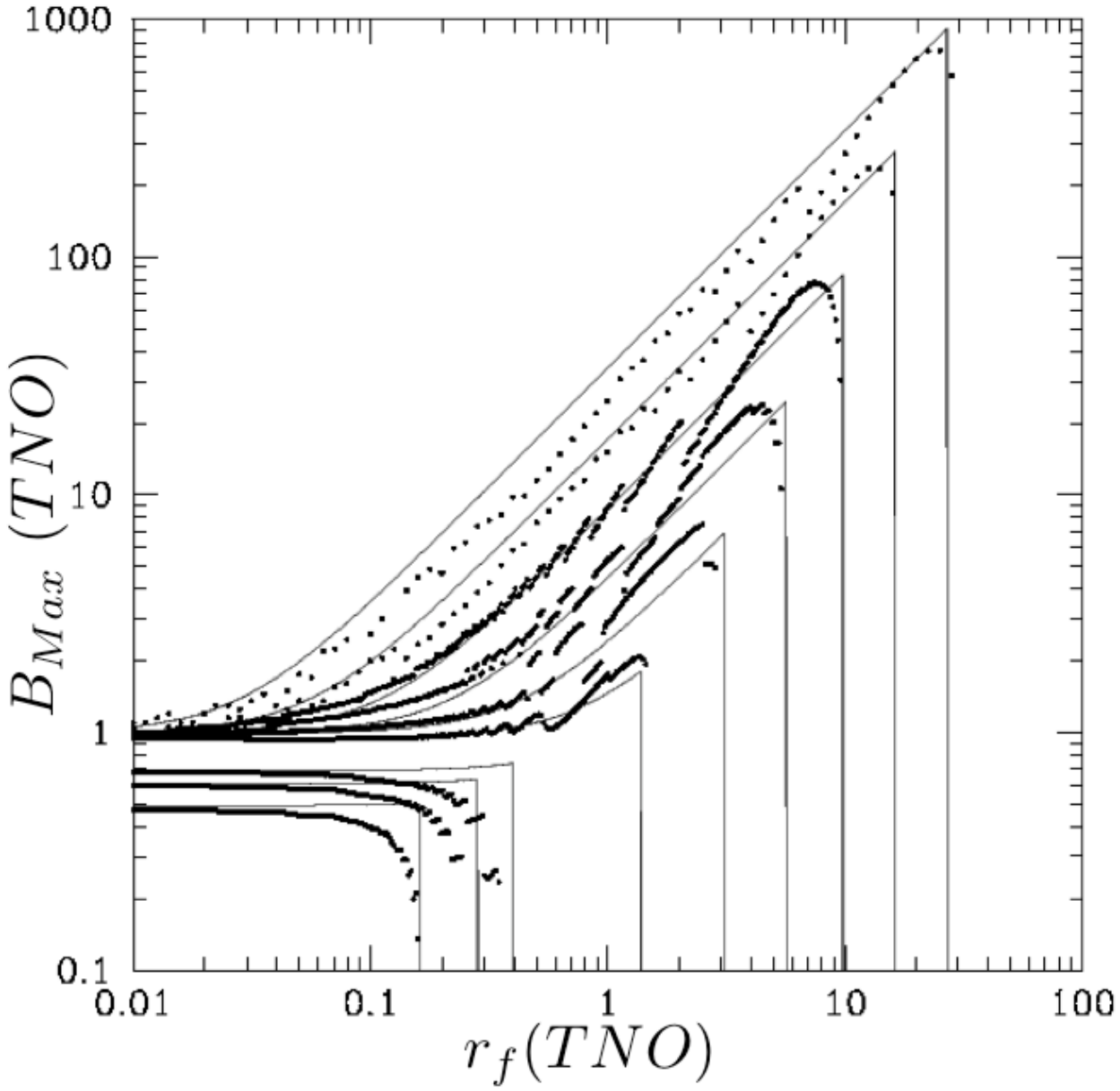

Fig. 8.— The curves show the maximum detectable impact parameter B_{max} as a function of the Fresnel scales r_f in units of TNO radius r, for various values of the RMS. Those below the B_{max}=1 limit have a $\log_{10}$(RMS) of -.03, -.05, and -.07 from bottom to top. Those above start at -.25 and increment by -.25 until $\log_{10}$(RMS)= -1.5. The fits provide a functional form for B_{max}.

6. Discussion

An important conclusion of our study, which is demonstrated in Figure 8, is that highly sensitive observations can detect stellar occultations with separations between the source and occulter that are several orders of magnitude greater than the radius of the TNO. Thus a simple geometric analysis would greatly overestimate the surface density of TNOs for a given occultation event rate. With the functional form of B_{max} we can now adopt models for the frequency, radius, and distance distributions of TNOs in a region of space and integrate over all radii and distances to predict the expected detection rates in future occultation surveys.

The usefulness of designing a functional form of B_{max} is the expedience of no longer having to do a standalone analysis of detectability for individual surveys. The function B_{max} acts as a library equipped with all previously calculated maximum impact parameters for every conceivable occultation event. By considering all physical parameters pertinent to occultation in advance, the plausibility, quality, and potential results of TNO surveys can be determined beforehand to aid in or detract from their executions.

REFERENCES

Bernstein G. M., Trilling D. E., Allen R. L., Brown M.E., Holman M., & Malhotra, R. , 2004. AJ 128, 1364.

Cooray A. , 2003. ApJ589, L97-L100.

Cooray A. & Farmer A. J. , 2003. ApJ587, L125-L128.

Duncan, M., Quinn, T., & Tremaine, S. , 1988. ApJ, 328, L69

Jewitt, D., & Luu, J. , 1993. Nature, 362, 730

Levison H. F., Dones L., Chapman C. R., Stern S. A., Duncan M. J., & Zahnle K. , 2001. Icarus 151, 286-306.

Malhotra R. , 1995. AJ 110, 420.

Nihei T. C., Lehner M. J., Bianco F. B., King S.-K., Giammarco J. M., & Alcock C. , 2007. ArXiv astro-ph/0703460v2.

Oort J.H. , 1950. Bull. Astron. Inst. Netherlands, 11, 91.

Roques F., Moncuquet M., & Sicardy B. , 1987. Astron J. 93, 1549-1558.

This manuscript was prepared with the AAS LaTeX macros v5.2.